Efficient Thin-Film CdS-MoS2-rGO Photocathode Composite for Photoelectrochemical Hydrogen Evolution Reaction at Neutral pH

Mohammed Alsultan * , Ahmed Suhail , Mohammad Yonis , Hiyam Altaai

Posted Date: 27 January 2026

doi: 10.20944/preprints202601.2091.v1

Keywords: photoelecrochemical (PEC); hydrogen evolution reaction (HER); CdS; reduced graphene oxide (rGO); tri-composite; tafel plot

 doi:10.20944/preprints202601.2091.v1

Article

Efficient Thin-Film CdS-MoS_2-rGO Photocathode Composite for Photoelectrochemical Hydrogen Evolution Reaction at Neutral pH

Mohammed Alsultan [1,*], Ahmed Suhail [1,2], Mohammad Yonis [1] and Hiyam Altaai [3]

[1] Department of New and Renewable Energy, College of Science, University of Mosul, Mosul 41002, Iraq
[2] Wolfson Nanomaterials & Devices Laboratory, School of Engineering, Computing and Mathematics, University of Plymouth, Devon, PL4 8AA, UK
[3] Department of Biology, College of Science, University of Mosul, Mosul, 41002, Iraq
* Correspondence: mohamadfkaleel@uomosul.edu.iq

Abstract

In this work, a CdS–MoS_2–rGO thin-film photocathode was fabricated on FTO substrates via a single-ink drop–spin-coating method followed by annealing under N_2 atmosphere. Among the studied compositions, the film containing 86:9:5 wt% of CdS, MoS_2, and rGO exhibited the best photoelectrochemical performance. Under visible-light illumination from a 50 W halogen lamp (~0.25 sun) in neutral electrolyte, the optimized photocathode achieved a photocurrent density of 0.83 mA cm^{-2} at −0.75 V vs Ag/AgCl and retained approximately 96% of its initial current during 60 min of chopped-light operation. Electrochemical impedance spectroscopy revealed a reduced charge-transfer resistance (~120 Ω·cm^2), while the Tafel slope decreased to ~85 mV dec^{-1}, indicating enhanced charge transfer and hydrogen evolution kinetics. Hydrogen production was confirmed by gas chromatography, with an evolution rate of ~58.6 μmol h^{-1}. The improved performance is attributed to the synergistic roles of CdS as the light absorber, rGO as an electron-transport network, and MoS_2 as a cocatalyst. These results demonstrate the potential of the CdS–MoS_2–rGO architecture for photoelectrochemical hydrogen evolution under neutral conditions.

Keywords: photoelecrochemical (PEC); hydrogen evolution reaction (HER); CdS; reduced graphene oxide (rGO); tri-composite; tafel plot

1. Introduction

Photoelectrochemical (PEC) hydrogen evolution has attracted considerable attention as a sustainable route for converting solar energy into chemical fuel [1]. An effective PEC photocathode requires suitable band-edge alignment, efficient light absorption, rapid charge transport, and resistance to photocorrosion under aqueous conditions [1,2]. Among visible-light-responsive semiconductors, cadmium sulfide (CdS) has been widely investigated due to its appropriate band gap and sufficiently negative conduction band edge for proton reduction [2,3]. However, pristine CdS often suffers from severe photocorrosion and rapid electron–hole recombination, which limit its long-term stability and practical application [3,4].

Various strategies have been explored to overcome these limitations, including coupling CdS with cocatalysts and conductive supports to improve charge separation and suppress recombination [4,5]. In particular, molybdenum disulfide (MoS_2) has emerged as an attractive non-precious cocatalyst for the hydrogen evolution reaction (HER) [6,7]. The edge sites of MoS_2 provide near-optimal hydrogen adsorption energy, while metallic or defect-rich regions can further enhance electron transfer kinetics [7,8]. Nevertheless, MoS_2 alone exhibits limited light absorption and charge transport capability, necessitating integration with suitable photoabsorbers and conductive scaffolds [8,9].

 doi:10.20944/preprints202601.2091.v1

Reduced graphene oxide (rGO) is frequently employed as a conductive support due to its high electrical conductivity, large surface area, and ability to form percolating networks that facilitate electron transport [10,11]. When combined with semiconductors, rGO can act as an efficient electron extraction layer, reducing charge accumulation and mitigating photocorrosion [11,12]. The incorporation of rGO into composite photocathodes has therefore been shown to improve both photoelectrochemical activity and operational stability [12,13].

In this context, constructing a ternary composite that integrates CdS as the light absorber, rGO as the electron transport network, and MoS_2 as the HER cocatalyst represents a rational approach to enhance PEC hydrogen evolution [9,13,14]. Such a configuration is expected to promote vectorial charge transfer, where photogenerated electrons are extracted from CdS, transported through rGO, and consumed at MoS_2 catalytic sites [14,15]. At the same time, the presence of rGO and MoS_2 can suppress photocorrosion of CdS by alleviating interfacial charge accumulation [12,15]. Recent studies have demonstrated that CdS-based photocathodes can achieve enhanced hydrogen evolution performance when coupled with suitable cocatalysts and conductive supports. In particular, MoS_2 has been widely reported as an efficient and earth-abundant cocatalyst for proton reduction, while reduced graphene oxide plays a key role in facilitating charge transport and suppressing recombination. Building on these findings, the present work explores a CdS–MoS_2–rGO composite system to improve photoelectrochemical activity and stability under neutral pH conditions [2–4].

In the present work, a CdS–MoS_2–rGO thin-film photocathode was fabricated using a simple solution-based drop–spin-coating method followed by thermal treatment under nitrogen atmosphere. The photoelectrochemical performance of the ternary system was systematically compared with binary and single-component control films under neutral pH conditions. Special attention was given to charge-transfer kinetics, interfacial properties, and operational stability. The results provide insight into the synergistic roles of each component and demonstrate the potential of the CdS–MoS_2–rGO architecture for PEC hydrogen evolution in mild aqueous environments.

2. Materials and Methods

All chemicals were of analytical grade and used without further purification. Natural graphite flakes, potassium permanganate ($KMnO_4$), sulfuric acid (H_2SO_4), hydrochloric acid (HCl), hydrogen peroxide (H_2O_2, 30%), cadmium nitrate tetrahydrate ($Cd(NO_3)_2{\cdot}4H_2O$), sodium molybdate dihydrate ($Na_2MoO_4{\cdot}2H_2O$), thiourea, ethanol, and aqueous ammonia (25–28 wt%) were purchased from commercial suppliers such as Sigma-Aldrich and Thermo Fisher Scientific. Fluorine-doped tin oxide (FTO, 15 Ω sq^{-1}) glass substrates were cut into 2 × 2 cm^2 pieces and used as conductive supports.

2.1. Preparation of Graphene Oxide (GO)

Graphene oxide (GO) was prepared using a modified Hummers method reported in the literature [1,2]. In a typical procedure, graphite flakes were dispersed in concentrated H_2SO_4 under continuous stirring while maintaining the temperature below 10 °C. $KMnO_4$ was gradually added to the suspension, followed by controlled heating to 35–45 °C and stirring for 2 h. The reaction mixture was then cooled and carefully diluted with ice–water, and the reaction was quenched by the slow addition of H_2O_2 until a bright-yellow suspension was obtained. The resulting product was washed repeatedly with dilute HCl and deionized water until near-neutral pH was reached. The final GO dispersion was obtained by sonication and centrifugation, yielding a stable aqueous suspension (~3.5–4 mg mL^{-1}).

2.2. Preparation of FTO Substrates

Prior to film deposition, FTO substrates were sequentially cleaned by ultrasonication in acetone, isopropanol, and deionized water for 10 min each. The substrates were dried under nitrogen flow and subsequently treated with UV–ozone for 15 min to enhance surface wettability. A brief plasma cleaning step was applied to obtain a hydrophilic surface suitable for uniform thin-film deposition.

 doi:10.20944/preprints202601.2091.v1

2.3. Preparation of CdS–MoS_2–rGO Composite Ink

The composite precursor ink was prepared by dissolving calculated amounts of $Cd(NO_3)_2 \cdot 4H_2O$, $Na_2MoO_4 \cdot 2H_2O$, and thiourea in deionized water under stirring until a clear solution was obtained. The quantities listed in Table 1 were calculated based on the target wt% ratios of CdS, MoS_2, and rGO at a fixed total solid loading.The pH of the solution was adjusted to 10.2 using aqueous ammonia, and the mixture was aged for 15 min to form metal–thiourea complexes. Thiourea was used in tenfold molar excess relative to the total metal content to ensure complete sulfurization during thermal treatment [3,4]. Ethanol was then added to obtain an ethanol–water co-solvent ratio of 85:15 (v/v). A measured volume of GO dispersion was introduced to achieve the desired rGO weight percentage in the final composite. A trace amount (0.01–0.03 wt%) of poly(vinylidene fluoride) (PVDF) was added as a binder to improve film adhesion. The final ink was sonicated for 30 min to ensure homogeneity(see table one).

Table 1. Calculated A,B,C,D composite component in X 10 mL ink, (1.2 mg mL^{-1}), EtOH:H_2O 85:15 v/v.

Sample	CdS (wt%)	MoS_2 (wt%)	rGO (wt%)	*m*(CdS) (mg)	*m*(MoS_2) (mg)	*m*(rGO) (mg)	$Cd(NO_3)_2$ (mL)	Na_2MoO_4 (mL)	GO (4mg mL^{-1}) (µL)	water (mL)	EtOH (mL)	Thiourea† (mg)
a (93:5:2)	93.0	5.0	2.0	11.16	0.60	0.24	0.772	0.037	60	0.690	8.435	61.6
b (96:3:1)	96.0	3.0	1.0	11.52	0.36	0.12	0.797	0.022	30	0.680	8.465	62.4
c (97:2:1)	97.0	2.0	1.0	11.64	0.24	0.12	0.806	0.015	30	0.679	8.465	62.5
d (86:9:5)	86.0	9.0	5.0	10.32	1.08	0.60	0.714	0.067	150	0.718	8.345	61.5
Ctrl 1 (0/0/100)	0.0	0.0	100	0.0	0.0	12.0	0.0	0.0	3000	1.500	5.495	0.0
Ctrl 2 (95/0/5)	95.0	0.0	5.0	11.40	0.0	0.60	0.789	0.0	150	0.711	8.345	60.1
Ctrl 3 (0/95/5)	0.0	95.0	5.0	0.0	11.40	0.60	0.0	0.712	150	0.788	8.345	54.2

† Thiourea amount corresponds to tenfold molar excess relative to total metal content.

The four compositions investigated in this work were selected to systematically evaluate the effect of varying MoS_2 and rGO contents while maintaining CdS as the primary light absorber. Increasing MoS_2 content provides additional catalytic edge sites for hydrogen evolution, whereas rGO enhances charge transport and suppresses recombination. By adjusting the relative proportions of these components, the compositions allow identification of an optimal balance between light absorption, electron transport, and catalytic activity. This approach enables meaningful comparison of structure–performance relationships within the ternary system. Pure CdS and pure MoS_2 films were experimentally attempted on FTO substrates; however, both exhibited poor mechanical stability and irreproducible photoelectrochemical behavior due to delamination under operating conditions. Therefore, rGO-supported binary films were employed as reliable and stable control samples for comparative analysis.

2.4. Film Deposition and Thermal Treatment

The composite ink was deposited onto pretreated FTO substrates using a drop–spin-coating technique. Each film was formed by three successive coating cycles at 3000 rpm for 60 s, with

 doi:10.20944/preprints202601.2091.v1

intermediate soft-baking at 110–120 °C to remove residual solvent. After the final coating, the films were annealed under flowing nitrogen using a stepwise heating program (90–120 °C, 160 °C, and 210–230 °C) to convert the metal–thiourea complexes into crystalline CdS and MoS_2 and to reduce GO to rGO [3–5].

2.5. Characterization Techniques

X-ray diffraction (XRD) patterns were recorded using Cu Kα radiation (λ = 1.5406 Å) to identify crystalline phases. Surface morphology was examined by field-emission scanning electron microscopy (FE-SEM). X-ray photoelectron spectroscopy (XPS) was performed to analyze surface chemical states. UV–visible absorption spectra were collected using a UV–Vis spectrophotometer in the range of 400–800 nm. Film thickness was measured using a stylus profilometer, and electrical conductivity was determined by a four-point probe method.

2.6. Photoelectrochemical Measurements

Photoelectrochemical measurements were carried out in a three-electrode configuration using a quartz cell. The CdS–MoS_2–rGO/FTO film served as the working electrode, a platinum mesh was used as the counter electrode, and an Ag/AgCl (3 M KCl) electrode was employed as the reference electrode. The electrolyte consisted of 0.5 M Na_2SO_4 adjusted to pH 7.0. Prior to measurements, the electrolyte was purged with nitrogen for 30 min. Illumination was provided by a 50 W halogen lamp corresponding to approximately 0.25 sun intensity. Linear sweep voltammetry, chronoamperometry, and electrochemical impedance spectroscopy were performed under dark and illuminated conditions. Hydrogen evolution was quantified using gas chromatography.component in X 10 mL ink, (1.2 mg mL^{-1}), EtOH:H_2O 85:15 v/v.

ǂ Thiourea amount corresponds to tenfold molar excess relative to total metal content.

Aliquots of CdS-MoS_2 solution were add to absolute EtOH yielding ethanol:water co-solvent ratio of 85:15 (v/v). in order to control thickness limitation and suppress cracking through the coating films on FTO glass across three coats, the total solid loading was set up to (1.0-1.2 mg mL^{-1}). Then the ethanoic GO dispersion was added to obtain ((from 1 to 5 depends to film control) wt % GO) in final composite; typically, (6-10 µL) ink sufficed to thin film (modified by coat count). Trace of (0.01 -0.03 wt%) amount of poly(vinylidene fluoride) (PVDF) binder was to improve film adhesion on the FTO glass substrate. (relative to projected film composite) was add and the mixture sonicated to 30 min to obtain homogenous ink[5,11,12].

2.4. CdS-MoS_2-rGO Film and Other Control Films Deposition (Three Thin Coats) and Thermal Conversion

Finally, the composite ink was drop-cast onto FTO slide and immediately spun-coated three times. Each coat at 3000 rmp for 60 and then soft-baked at (110-120) °C to remove solvent and setting binder prior to the next application. After the third the slide's film was annealed in flowing of N_2 gas films were annealed in flowing N_2 according to procedures; from 90-120 °C (10 min.) → 160 °C (10 min) → 210-230 °C (45 min) (ramp≈ °C min^{-1}). The above steps reduce GO→ rGO, covert CdS-thiourea complexes to CdS) and form catalytically active MoS_2 while minimizing oxidation therefore annealing in air is not recommended[13–15].

2.5. Measurement Techniques; X-Ray Powered Diffraction (XRD)

The XRD of CdS-MoS_2-rGO, and other control samples were carried out on GBC MMA XRD at wavelength of 1.54 Å while the supplied voltage and current were kept at -40 kV, 25 mA respectively. **Scanning Electron Microscope (SEM)**; The sample's surface morphology examined via JEOL-7500F field emission. The procedure operated at 5 kV and 8 mm working distance. **X-ray photoelectron spectroscopy (XPS)** it was performed on PHI660 using a monochromatic Mg Kα X-ray was used as a beam source. The survey scan was 200 eV pass energy with high-resolution regions on (C 1S, O 1s, Cd 3d, S 2p, Mo 3d). **UV-Vis spectrum** recorded by UV-1800 SHIMADZU in range (400 -800) nm.

 doi:10.20944/preprints202601.2091.v1

Film **thickness and conductivity**; thickness measurement was done through a Vccco Dektak 150 profilometer while conductivity measured via four points probes (Jandel Engineering Ltd, UK).

2.6. Photoelectrochemical Measurement

For (PEC) experiment; A quartz cell (5 x 5 x 5 cm) was fully-closed and placed inside closed box as comprised to faraday cage. was placed inside a closed cabinet that comprised a Faraday cage. A conventional three-electrode photoelectrochemical cell was used, consisting of the CdS–MoS_2–rGO/FTO working electrode, a platinum mesh counter electrode, and an Ag/AgCl reference electrode..The prepared thin film was used as working electrode (WE) after pasted with copper wire at the top edge of FTO-Coated glass by silver glue. Then Epoxy-resin was covered the all age of FTO –film including pasted area. Pt- Mesh (1 x 2 cm) was acted as counter electrode(CE). While Ag/AgCl with aqueous salt bridge (contained KCl, 3M) performed as references electrode(RE)., 0.5 M Na_2SO_4 adjusted to pH 7.0 by phosphate buffered. The neutral electrolyte was previously bubbled with N_2 gas for 30 min before each experiment. The electrolyte was bubbled with N_2 gas for 30 min before each experiment. The **cyclic voltammetry (CV)**, **chronoamperograms** and **EIS** were tested with and without light illumination. I.R bandpass filter (315-710 nm) was placed at 1.5 cm after the light source. Sun light simulator of (50 watts,0.25 sun) was used as source light Which it simulated 100 mW cm^{-2}. For more details, LSV were recorded with and without illumination at rage of (0.0 -1.25) V *vs* Ag/AgCl (3 M KCl) with scan rate 5 mVs^{-}. More negative potential ≈ −1.30 V *vs* Ag/AgCl could resulting in photocorrosion CdS in containing film[16]. The experiments of Chronoamperograms**;** The measurements performed also with, and without illumination at potential of -0.75 V *vs* Ag/AgCl with chopped-light each two min. for 60 min. Additional potentials tests carried out at more negative bias range (-0.8 - -0.95) V to obtain more photocurrent efficiency[16]. In some experiments hydrogen evolution gas were connected GC for H_2 quantification where Faradic efficiency was calculated. EIS was carried out under illumination at external bias of -0.82 *vs* Ag/AgCl at frequencies rage of (10-200) KHz. EIS model EC-Lab V10.44 and Z-View 3.5C software were utilized to collect data, spectrum and fitting respectively[17]

3. Results and Discussion

3.1. Linear Sweep Voltammetry (LSV) and Photocurrent Density

Figure S1 displayed (LSV) of CdS-rGO-MoS_2 at different ratios as well as other control films according Figure 1 calculations. While pure CdS and pure MoS_2 films prepared on FTO were found to be mechanically unstable under PEC conditions, exhibiting delamination and irreproducible current responses; therefore, rGO-supported binary films were employed as reliable control electrodes.Table 2 showed the outcomes results of LSV. As can be seen from table 2 and Figure 1: under the dark state all under dark conditions, all working electrode's film show only limited electrochemical current densities with more negative potential. However, the ternary film CdS-MoS_2 –rGO showed slight kinetic advantage in the dark current densities. It approximately increases from (193-209) μA cm^{-2} for film from a-d (86:9:5 CadS; MoS2; rGO). And the onset potential moved from -0.68(a) to -0.64 V (d). In contrast rGO control film remains has lowest current density (~30 μA cm^{-2}). Other control films Cntr.2 and contr.3 showed higher current densities reached (150 and 160) μA cm^{-2} respectively with more negative potential than ternary film.

 doi:10.20944/preprints202601.2091.v1

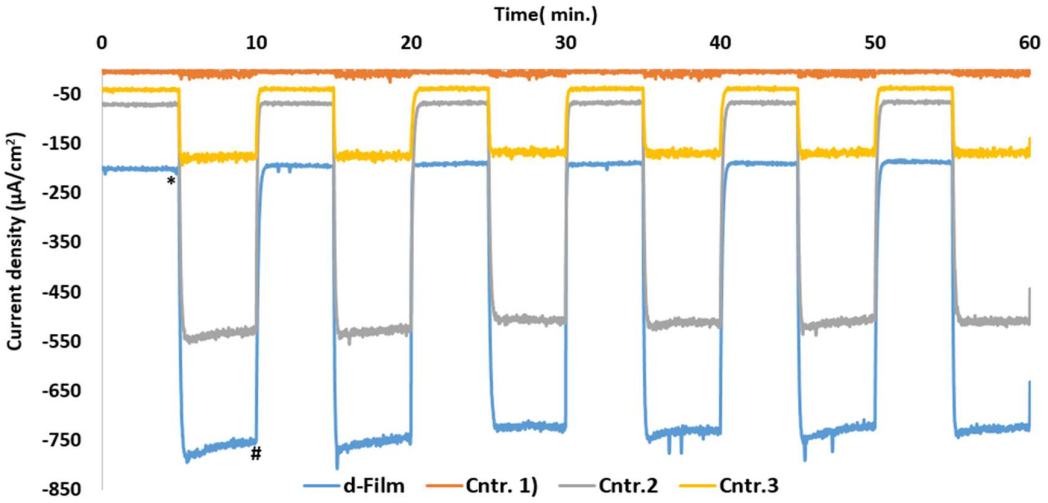

Figure 1. Chronoamperograms at 0.75 V (vs Ag/AgCl) over 1 h of operation, with and without light illumination (0.25 sun), of FTO slides coated with thin films of; d-film, Cntr.1, Cntr.2 and Cntr.3 (*='light on', #='light off').

Cathodic current densities are plotted as negative values following the conventional representation for photocathodes, where hydrogen evolution occurs under reductive bias..Under light illumination, the photocurrent density of ternary electrodes increased by 516, 561, and 627 μA cm^{-2} for a-c respectively. Then IT reached the maximum of 836 μA cm^{-2} for d. relative to other controls d-film is markedly superior. It higher rGO by 8.72 times, and higher MoS2-rGO and CdS-rGO by 4.1 and 3.0 times respectively under identical conditions. These data demonstrate that light when light be absorbed by CdS, it not yes sufficient for HER. Therefore, the presence of electrons transport-accelerator along rGO network and provided reaction eges csites at MoS_2 are essential to sustain the HER centers[18,19]. In addition, illumination shifted the onset potential to less negative values lowering the HER overpotential. For example, the onset optional moved from -0.68 → 0.54 V in a-film, -0.66→ -0.52 in b-film, -0.65→ 0.52 V in c-film and -0.64 → -0.49 V in d-film. d –film (86:9:5) was sufficient to drive rapid extraction and in-plane conduction, MoS_2 (~9 wt%) provides abundant edge sites without excessive shading, while CdS remains main light absorber. As we tried further increase rGO in rGO/MoS_2 or leads to induce electronic traps or parasitic absorption[20].

Table 2. shows the outcomes results of LSV.

Samples & controls film	Dark current density (μA·cm^{-2})	Light current density (μA·cm^{-2})	Dark onset potential (V)	Light onset potential (V)
a)	193	709	−0.68	−0.54
b)	196	757	−0.66	−0.52
c)	201	803	−0.65	−0.52
d)	209	836	−0.64	−0.49
Cntr.1 (rGO)	30	86	−0.82	−0.73
Cntr.2 (CdS–rGO)	160	643	−0.72	−0.55
Cntr.3 (MoS_2–rGO)	150	592	−0.75	−0.61

 doi:10.20944/preprints202601.2091.v1

3.2. Chronoamperometric Investigations

Next step was to investigate chonoamperometry of CdS-MoS_2-rGO photocathode film; under bias of -0.75 vs Ag/AgCl, and chopped light each 5 min. for 1 h. as can be showed in Figure 1 When the light was switched on d-Film (CdS–MoS_2–rGO) showed highest and most stable cathodic photocurrent density. delivered the highest and most stable cathodic photocurrent density at ≈ −0.78 mA cm^{-2}, dark baseline current reached near −0.22 mA cm^{-2}. The on/off contrast (ΔJ) was around (−0.56 mA cm^{-2}). which it exceeds all other controls (see Table 3). For example, the cathodic current of Cntr.1 showed very limited substantial current traces even in the light. In Cntr.3 control film the current was increased from 44μA to 184μA when the light was switched meaning the light boost PEC system by 144 μA. in Cntr.2 the light enhanced the system by 467 μA when raised the current from (72 to 539) μA. During over 60 min of PEC operation, d-film only lost about 4% of its photocatalyst efficiency of its initial light on current. Which made it favorable film based on CdS photocathodes under long-continuous operation. Mechanistically, the superior performance of d-film related to complementary function of each continent; CdS nanoparticle providing strong light adsorption, MoS2 supplying sufficient active sites for HER and enhancing low-resistance way for photogenerated electrons.

Table 3. summarized outcomes results from(EIS) fitting data.

Label	Film type	R_0 (Ω·cm^2)	Rct (Ω·cm^2)	QCPE (μΩ^{-1}·cm^{-2}·s^n ×10^{-4})	nCPE	Cdl (μF·cm^{-2})	kct (s^{-1})
(i)	rGO — dark	40	450	1.5	0.82	6	370
(ii)	rGO — light	39	360	2.0	0.85	7	397
(iii)	MoS_2–rGO — dark	38	310	2.2	0.86	7.5	430
(iv)	MoS_2–rGO — light	38	220	2.8	0.88	9	505
(v)	CdS–rGO — dark	38	240	2.5	0.88	8.5	490
(vi)	CdS–rGO — light	37	155	3.3	0.90	10	645
(vii)	CdS–MoS_2–rGO — dark	37	260	3.0	0.90	9.5	405
(viii)	CdS–MoS_2–rGO — light	36	120	3.8	0.92	11	758

Neutral pH operation offers a practical compromise between activity and stability for CdS-based photocathodes. Under these conditions, rapid electron extraction by rGO and catalytic turnover at MoS_2 edge sites suppress charge accumulation and photocorrosion, enabling sustained hydrogen evolution. This behavior defines the operational advantage boundary of the CdS–MoS_2–rGO system under mild aqueous environments.

3.3. UV-Visible and X-Ray Diffraction (XRD) Studies

Figure S.2 UV-Vis-spectrum of d-film(CdS-MoS_2-rGO), Cntr.2 (CdS-rGO), Cntr.3(MoS_2) and Cntr.1 rGO Among all films absorptions, d-film (CdS–MoS_2–rGO) showed highest and broadest absorption at visible range which it consistent within combined contributions; of direct-gap absorber (CdS), transmission excitonic of MoS_2 layers, and the broadband of rGO. D-film showed suitable absorption range till ≈675 nm[21]. While Cntr.2(CdS–rGO) spectrum remain below d-film curve absorbance. Which it reflected the absence of; MoS_2 excitonic features and the reduced strength of oscillator upon partial rGO dilution[22]. The Cntr.3 (MoS_2–rGO) spectrum displays the characteristic MoS_2 excitonic resonances at range of 600–700 nm region[23]. Cntr.1 (rGO) provided broadband background which enhances light harvesting. Especially when it combined with semiconductors like CdS. The ternary d-film showed higher optical density at (A_{450}, A_{550}, A_{650}) than any other controls. Which it indicated the improvement of solar-light harvesting across blue–green regions. Thus, the optical absorbance were follow the ordered-Film > Cntr.2 ≳ Cntr.3 > rGO mirrors the photocurrent hierarchy observed. The rGO film exhibits single broad (002) peaks at 24.8° which indicated that

 doi:10.20944/preprints202601.2091.v1

graphene oxide fully reduced to rGO. Another weak peak at 2θ ≈ 43–45° is assigned to the (100) indicated modest of hexagonal in-plane order rGO[24]. In control Cntr.2 (CdS-rGO) displayed peaks at 2θ ≈ 24.8° (100), 26.5° (002), 28.2° (101), 36.7° (102), 43.9° (110), 47.8° (103), and 51.8° (112), related to hexagonal CdS. Cntr.3 (MoS_2-rGO) showed dominant 2H-MoS_2 (002) peaks at ~14.4° (002). The optical absorption bandgap behavior of the prepared samples was evaluated using UV–Vis spectroscopy according to Tauc method, as shown in the Supplementary Information (S.3)and summarized in table (S.4). in more details, the CdS–rGO film showed a direct bandgap of 2.26 eV, which it is significantly agreement with previously reported values for CdS-based materials [25]. However, when MoS_2 and rGO are introduced, the band gap of the CdS–MoS_2–rGO composite slightly decreases to around 2.22 eV[26]. Such a change is likely due to interactions of CdS/MoS_2 interface film that improved charge transport through the rGO framework. For comparison purpose, the MoS_2–rGO control sample shows an indirect band gap of approximately 1.48 eV, consistent with multilayer MoS_2. This behavior is observed usually in hybrid CdS/MoS_2 systems due to attributed to interfacial electronic interactions. while no clear band-gap edge can be identified for rGO due to its semi-metallic nature[27].

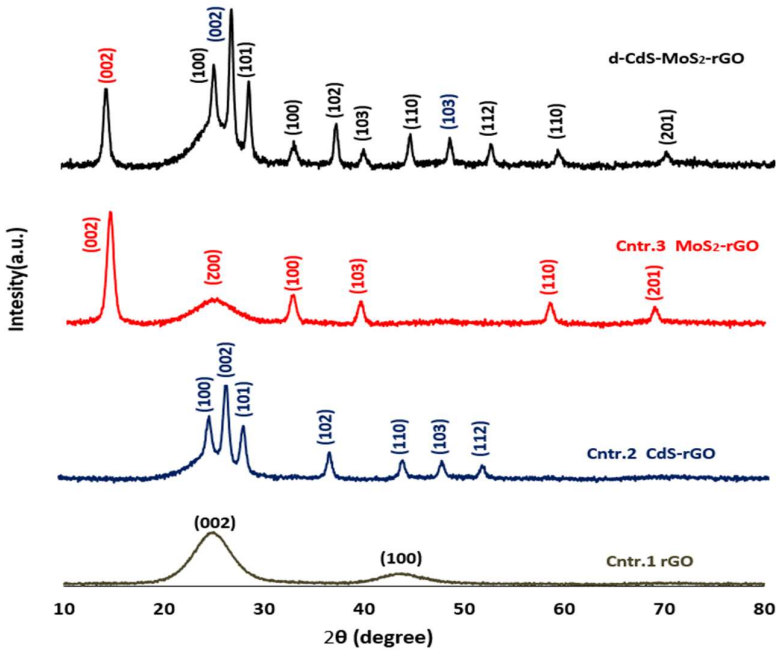

Figure 2. Powder X-ray diffraction (XRD) of Cntr.1 (rGO), Cntr.2(CdS-rGO),Cntr.3 (MoS_2-rGO) and d-(CdS-MoS_2-rGO) film.

accompanied with weak peaks at ~32.7°(100) , ~39.5 (103) and 58.5° (110). In addition rGO peak appeared at 2θ ≈ 24.8° (002). However, the ternary d-(CdS-MoS2-rGO) Film contains reflections peaks of both CdS and MoS_2 on top of the rGO background. Which confirmed the successful co-assembly without additional crystalline peaks.

3.4. SEM Measurement and Surface Morphology

Figure 3 shows the SEM images of a) rGO , b) rGO-CdS , c) rGO-MoS2 and d) rGO-CdS-MoS2 films rGO film has wrinkled sheets which the corrugation produced inter sheets with high roughness factors which resulting in increased the electrochemically of accessible area, prepare edge-defect site for heterogeneous nucleation, and creating continuous sp^2-carbon network for lateral electrons transport. In rGO–CdS film CdS nanoparticles uniformly decorated rGO scaffold. The high density of nucleation centers on rGO can maintain the electrolyte access, reduce light-blocking of the carbon

 doi:10.20944/preprints202601.2091.v1

network, and provide numerous CdS/rGO hetero-interfaces resulting in facilitate electron transfer from photo-excited CdS into the conductive rGO. While in rGO–MoS_2 distinct flower reosettes can be observed at size of ~150–300 nm. which resulted in; providing edge-rich morphology that useful for HER activities. with clear inter-rosette spacing that limits restacking. This anisotropic, edge-rich morphology is advantageous for HER. While unsaturated S-edge sites dominate the exposed area. In addition, rGO backbone provided an electron sink and mitigates charge buildup

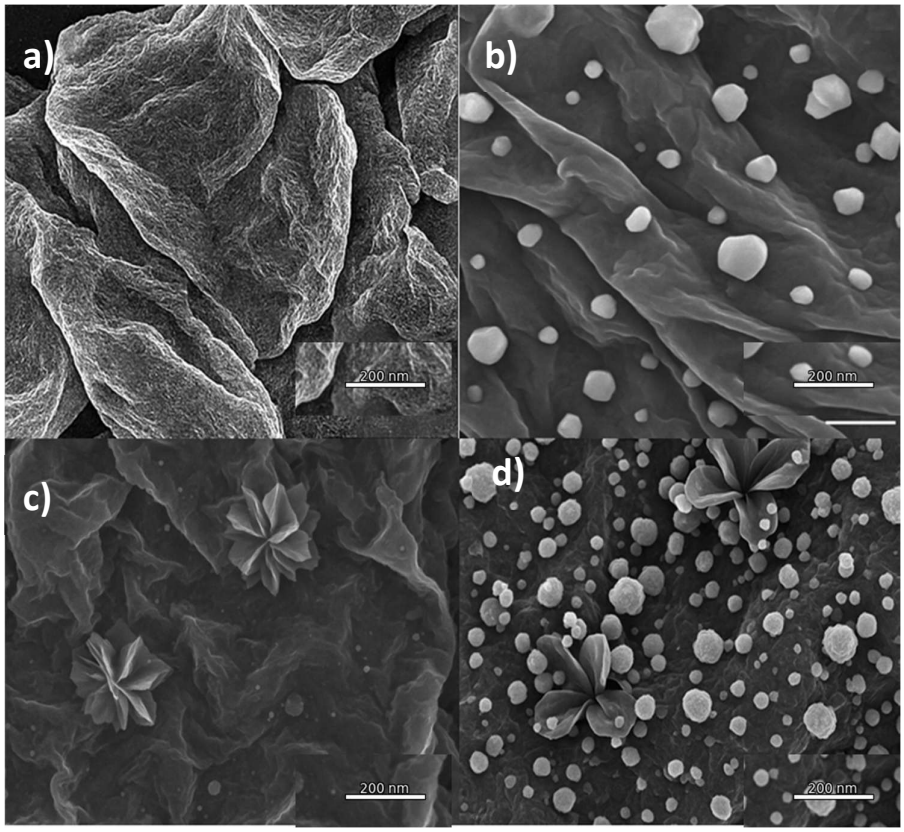

Figure 3. SEM image of a) rGO showed multilayers- wrinkled **(b)** rGO–CdS (CdS nanoparticles around (~40–120 nm) provided CdS/rGO heterojunctions; **(c)** rGO–MoS_2 flowered-like MoS_2 rosettes arround (~150–300 nm) exposed edge-rich catalytic sites; **(d)** tri-composites rGO–CdS–MoS_2 film.

3.5. X-Ray Photoelectron Spectroscopy

As can be seen in Figure 4 a) C 1s — rGO envelope showed peaks at (284.7, 285.5, 286.5, 287.6, (288.9 and 290.8) eV which contributed to Sp3(in C-C), Sp2(C=C), C-O, C=O, C-C=O and π-π^* respectively [29]. In b) O 1s — rGO a three components are observed at (531.4, 532.6 and 534.3) eV belong to C=O, C-O and C-C=O respectively [25].In c) Cd 3d- CdS XPS a clean Cd+2 doubled peaks at 405 and 411.7 eV which assign to Cd 3d5/2 and Cd $3d_{3/2}$ respectively [30].In d) S 2p-CdS envelope it was observed two peaks at (161.6-162.8)eVand (163.6-163.9) eV relate a weak S^0/S–S shoulder S 2p-CdS and minor SOx due to its brief ambient exposure [31].In e) Mo-3d it was noted a doubled peaks at (229.5-232.7)eV due to electron configuration of Mo+4 with small low shoulder around 228.6 eV contributed to 1T-like/reduced Mo at S-vacancies. f) The S 2s –MoS_2 XPS spectra showed clean doubled cites at (162.0-163.2) eV with small widths [32]. 162.8) eV and (163.6-163.9) eV relate a weak S^0/S–S shoulder S 2p-CdS and minor SOx due to its brief ambient exposure [31].In e) Mo-3d it was noted a doubled peaks at (229.5-232.7)eV due to electron configuration of Mo+4 with small low shoulder around 228.6 eV contributed to 1T-like/reduced Mo at S-vacancies. f) The S 2s –MoS2 XPS spectra showed clean doubled cites at (162.0-163.2) eV with small widths [28]. In overall, the XPS

 doi:10.20944/preprints202601.2091.v1

investigation supports the efficient photo generated electron extraction from CdS into rGO and rapid delivery to MoS_2 edge sites, enhancing HER. XPS analysis was focused on the composite films to probe interfacial chemical states relevant to charge transfer, while reference-material XPS measurements are reserved for future detailed studies.

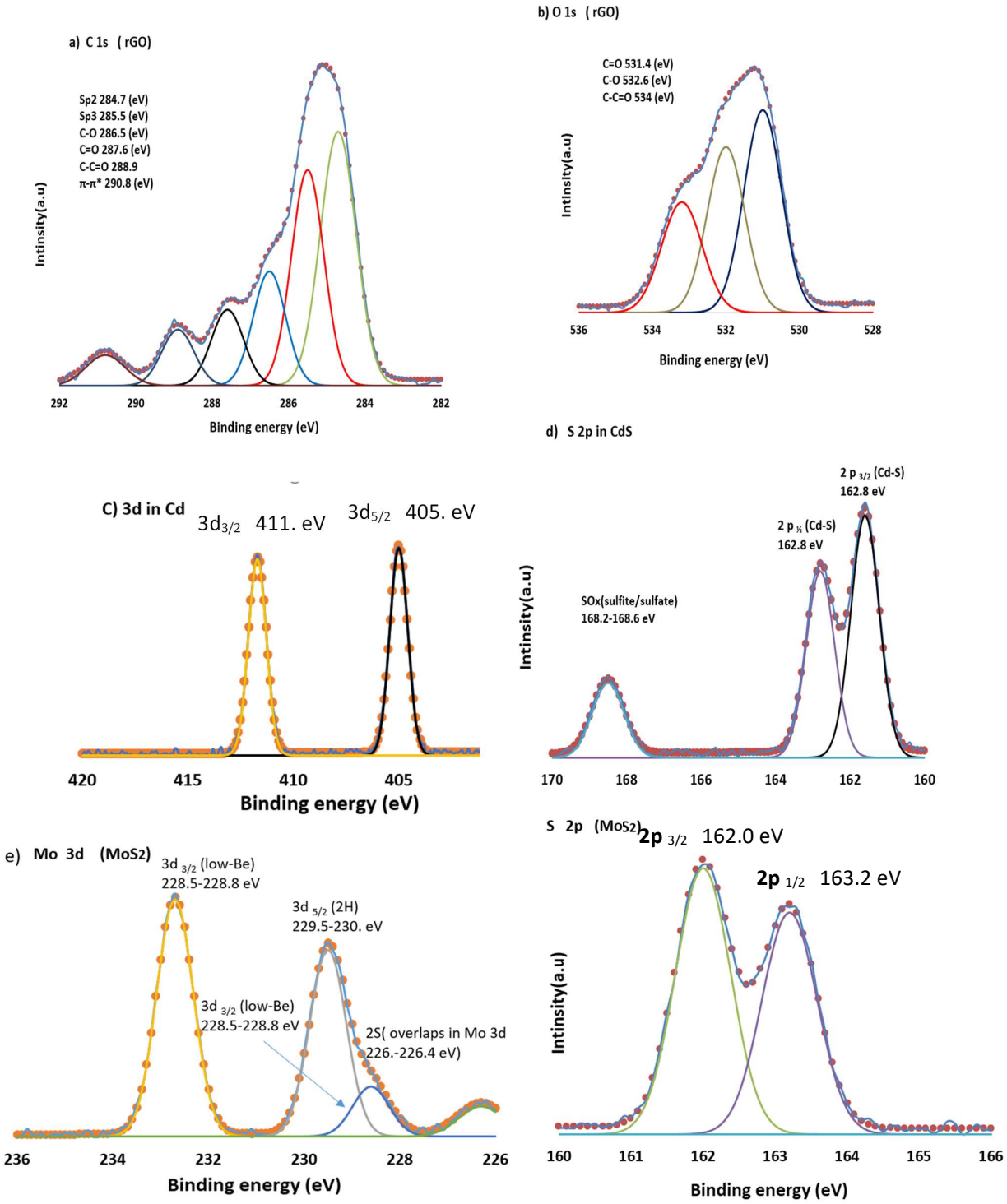

 doi:10.20944/preprints202601.2091.v1

Figure 4. XPS spectra of CdS-MoS_2-rGO film; a) C 1s and b) O1s related to rGO. C) and d) represent Cd-3d and S 2p-CdS respectively. While e and f represent Mo-3d and S 2p (MoS_2) resp.

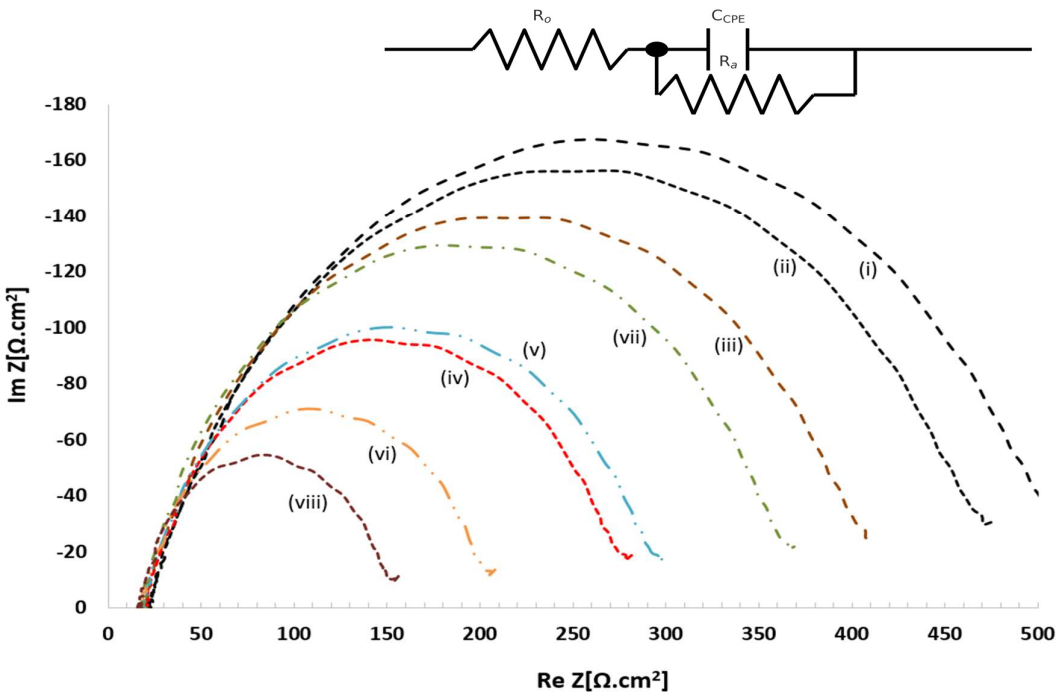

Figure 5. i -rGO in dark and ii- rGO in the light , (iii)-MoS_2-rGO in dark and (vii)-CdS-MoS_2-rGO-dark , and (v)-CdS-rGO-dark and (iv) MoS_2-rGO light), and vi-CdS-rGO light and finally viii-CdS-MoS_2-rGO. The inset electrical circuit model single-time constant Randles circuit type (Rs-R1-(R2‖CPE)).

3.6. Electrochemical Impedance Spectroscopy (EIS) & Tafel Plots Studies

Figure 5.a) shows Nyquist plots that labeled from (i-viii). Which it was fitted with an excellent match to equivalent electrical circuit model single-time constant Randles circuit type (Rs-R1-(R2‖CPE)) as can be seen in inset plot (b). At neutral pH , the low to intermediate frequencies processes refer to adsorption that involved transfer of ions (charge carriers) from the diffuse layer to the try-composite-photo-catalyst. Ro, and Ra represent adsorption resistance and interfacial charge transfer resistance respectively. Also it is an excellent match to equivalent electrical circuit model single-time constant Randles circuit type (Rs-R1-(R2‖CPE)) as can be seen in inset plot (b). At neutral pH , the low to intermediate frequencies processes refer to adsorption that involved transfer of ions (charge carriers) from the diffuse layer to the try-composite-photo-catalyst. Ro, and Ra represent adsorption resistance and interfacial charge transfer resistance respectively.

While the capacity of constant-phase element (CPE) involved Q and n parameters represents the non-ideal double layer and accounts for the depressed semicircle respectively. Table 3 summarized parameters reported by fitting Nyquist plots with an electrical equivalent circuit model [33].

Wher Ro represented resistance of uncompensated solution/electrolyte, while Rct denoted resistance of the charge-transfer at the electrode/electrolyte interfaces. QCPE and nCPE attributed to the constant-phase element with its exponential factor. Which it reflected capacitance behavior of interfacial non-ideal. Cdl is the capacitance of double-layer, and kct is the rate constant of apparent charge-transfer. It calculated from the reciprocal of Rct. However, the reduction value of Rct and

 doi:10.20944/preprints202601.2091.v1

higher of Cdl and kct under light illumination, indicated the facilitation of charge separation and interfacial charge transport enhancement in the ternary CdS–MoS_2–rGO film relative to binary or single-component controls[34]..

Table 3. summarized outcomes results from(EIS) fitting data.

Label	Film type	R_0 (Ω·cm²)	Rct (Ω·cm²)	QCPE (μΩ⁻¹·cm⁻²·sⁿ ×10⁻⁴)	nCPE	Cdl (μF·cm⁻²)	kct (s⁻¹)
(i)	rGO — dark	40	450	1.5	0.82	6	370
(ii)	rGO — light	39	360	2.0	0.85	7	397
(iii)	MoS_2–rGO — dark	38	310	2.2	0.86	7.5	430
(iv)	MoS_2–rGO — light	38	220	2.8	0.88	9	505
(v)	CdS–rGO — dark	38	240	2.5	0.88	8.5	490
(vi)	CdS–rGO — light	37	155	3.3	0.90	10	645
(vii)	CdS–MoS_2–rGO — dark	37	260	3.0	0.90	9.5	405
(viii)	CdS–MoS_2–rGO — light	36	120	3.8	0.92	11	758

For more details, (Ro) series resistance were varied gradually between (40 → 36 Ω·cm²). This decreasing value across the set, confirmed the differences in semicircle diameter primarily that can have reflected to the interfacial kinetics. In addition, under illumination Ra percentage (%) among all phot- electrodes decreased following the trend; rGO (−19%), MoS_2–rGO (−28%), CdS–rGO (−33%), and CdS–MoS_2–rGO (−53%). However, lowest Ra that obtained was belong to ternary electrode under light (121 Ω·cm²), Concomitantly, both Q and Cdl values were increased while the CPE exponent n was varied (0.82 → 0.92). which it indicates to more ideal capacitive behavior during photo-operation and provided largest electro-chemical active surface area (ECSA). The tri-light composites CdS-MoS2-Rgo also showed highest kinetic descriptor $k\_ct \approx (Rct \cdot Cdl)^{-1}$. Followed by CdS–rGO–light and MoS_2–rGO–light. Dependong on the equation $i_0 = RT/(nFRct)$ (n = 2), the exchange current density increased from 28 μA.cm-2 at rGO–dark to 107 μA.cm-2 at tri-light composites CdS-MoS_2-rGO[35].

Mechanistically, CdS provides light-carrier generation, rGO offers low charge resistance percolation network that extracts and delocalizes electrons. While and MoS_2 provided HER-active edge sites. This system exhibits smallest Rct, highest Cdl, and most ideal interfacial capacitive responses for HER photocathode performance.

As can be seen in S.5 when the light was switched on, the d) tri- CdS–MoS_2–rGO photocathode composite obtained lowest Tafel slope at (85 mV dec⁻¹). which it reflected the high accelerated interfacial hydrogen evolution kinetics among all other binary or single-component controls. Notably, even at dark d) tri-composite tafel slope remained small comparatively at (120 mV dec⁻¹) showing favorable charge-transfer pathways even in the absence of photocarriers. For comparison purpose, Cntr.2) CdS–rGO composite improved HER activity over pare rGO. When its tafel plots reached (110 and 140 mV dec⁻¹ under light and dark, respectively). Actually, Cntr.2 film confirmed when, photo-generation coupled with a conductive scaffold boosts the catalytic turnover. Other bi-composite MoS_2–rGO (Cntr.3) exhibits higher tafel plots performer reached (135 and 160 mV dec⁻¹ under light and dark). This results reflected the limited poor absorber as well as restricted electrons supplier. Thus, the trend of HER activity trend under light follows CdS–MoS_2–rGO » CdS–rGO > MoS_2–rGO. This is due to interplay synergistic among light absorption between charge transport, and catalytic processes that can suppress the recombination reaction through heterointerfaces.

The enhanced performance of the CdS–MoS_2–rGO photocathode can be understood in terms of band alignment and interfacial charge transfer. Upon illumination, photogenerated electrons in CdS are transferred to rGO due to its favorable Fermi level, which suppresses charge recombination.

 doi:10.20944/preprints202601.2091.v1

These electrons are subsequently delivered to MoS_2 edge sites, where proton reduction occurs efficiently. This charge-transfer pathway is consistent with the observed reduction in charge-transfer resistance and improved reaction kinetics.

Table 4. Charge-Transfer Resistance (Rct), Exchange Current Density (i_0), and Tafel Slope of d-film and other control films.

Sample	Rct (Ω·cm²)	i_0 (mA·cm⁻²)	Tafel slope (mV·dec⁻¹)
(i) rGO — dark	445	0.028	280
(ii) rGO — light	355	0.036	255
(iii) MoS_2–rGO — dark	332	0.041	211
(iv) MoS_2–rGO — light	217	0.058	176
(v) CdS–rGO — dark	242	0.053	146
(vi) CdS–rGO — light	157	0.083	126
(vii) CdS–MoS_2–rGO — dark	256	0.049	111
(viii) CdS–MoS_2–rGO — light	118	0.055	86

3.6. Gas Chromatography (GC) and Hydrogen Evolution Rates

As can be seen in Figure S.6 a confirmed distinct H_2 peaks was appeared at ≈2.0 min of retention time. These peaks related to d) CdS–MoS_2–rGO photocathode. However, under illumination, the film generates the largest H_2 rate reached to 58.6 μmol h^{-1}. While in the dark yielded rate up to 14.1 μmol h^{-1}. These results confirmed that visible-light excitation in CdS is essential to drive proton reduction while blank electrolyte produced only negligible hydrogen rate as expected. The high H_2 rates under light and lowest Tafel plots ensured the synergistic roles of the three components CdS-nanoparticles, rGO sheets and, MoS_2 which they generate electrons-holes, rapid extracting electrons with low resistances and edges served as competent her sites respectively. It can be concluded that d) tri : CdS–MoS_2–rGO film provide the optimum balance between photons absorption, carrier transport and catalytic turnover. rGO control film showed limited trace hydrogen evolution at both cases dark and light, while CdS-rGO and MoS_2-rGO exhibted (9.2 μmol h^{-1} dark, (41.2 μmol h^{-1}light) and (7.2 μmol h^{-1}dark (,(24 μmol h^{-1} light) respectively. The fast and stable photocurrent response under chopped illumination reflects efficient carrier separation and rapid electron extraction by the rGO network, consistent with the reduced Rct and enhanced capacitive behavior observed in EIS measurements. Although atomic-scale HRTEM characterization was not available, the combined SEM, XRD, XPS, and EIS results provide consistent evidence for effective heterojunction formation and interfacial charge transfer. The amount of evolved hydrogen was quantified using gas chromatography (GC). During PEC operation, the gas produced at the photocathode was collected and injected into the GC system for analysis. Hydrogen evolution rates were calculated from the measured peak areas using calibration with standard hydrogen gas. The moderate photocurrent density can be attributed to the low-intensity halogen illumination, neutral electrolyte, and thin active layer, while the high photocurrent retention (~96%) confirms good operational stability. The ABPE efficiencies of the different compositions do not show pronounced differences under the applied experimental conditions. This behavior can be attributed to the use of low-intensity illumination (0.25 sun) and neutral pH electrolyte, where the applied bias plays a dominant role in determining efficiency. While ABPE values are similar, clear differences in charge-transfer resistance and reaction kinetics are evident from EIS and Tafel analyses, indicating that the compositional optimization primarily enhances interfacial charge transport rather than bias-dependent efficiency. The amount of evolved hydrogen was quantified for all investigated samples under identical photoelectrochemical conditions using gas chromatography. The ternary CdS–MoS_2–rGO photocathode exhibited the

 doi:10.20944/preprints202601.2091.v1

highest hydrogen evolution rate, while the binary and single-component control films produced lower amounts of hydrogen. These results follow the same trend observed in the photocurrent and kinetic analyses, further supporting the structure–performance relationship among the different compositions.

3.7.. Applied-Bias Photon-to-Current Efficiency (ABPE)

ABPE efficiency for d) CdS-MoS_2-rGO film and other control films. Firstly, the potential converted to RHE instead of Ag/AgCl (3 M KCl) at 25 °C, by Equation[36]:

$V_{RHE} = V_{Ag/AgCl} + 0.210 + 0.059 \times pH$ ……..1

When ($V_{Ag/AgCl} = -0.75$ V) at (pH = 7), the V_{RHE} value be =(−0.077 V). then after, the applied-Bias Photon-to-Current Efficiency was calculated via equation[37]:

$\eta_{ABPE}(V) = |J(V)| \times (1.23 - V_{RHE}) / P_{in} \times 100\%$ ……2

(when η represent the efficiency , J the net photocurrent density in unit A/cm-2 (calculate substituted light current – dark current) and P_{in} represent the power simulated light sources in unit W.cm^-2 . After Substituted the numbers into the equation last equation, the efficiency can be calculated as can show in Figure 6.

Overall, the photoelectrochemical performance trends observed for the different compositions can be directly correlated with their structural and interfacial characteristics. Variations in MoS_2 and rGO content influence catalytic site density and charge-transport pathways, as reflected by changes in charge-transfer resistance, reaction kinetics, and hydrogen evolution rates. This consistent behavior across structural, electrochemical, and catalytic analyses establishes a clear structure–performance relationship within the CdS–MoS_2–rGO system.

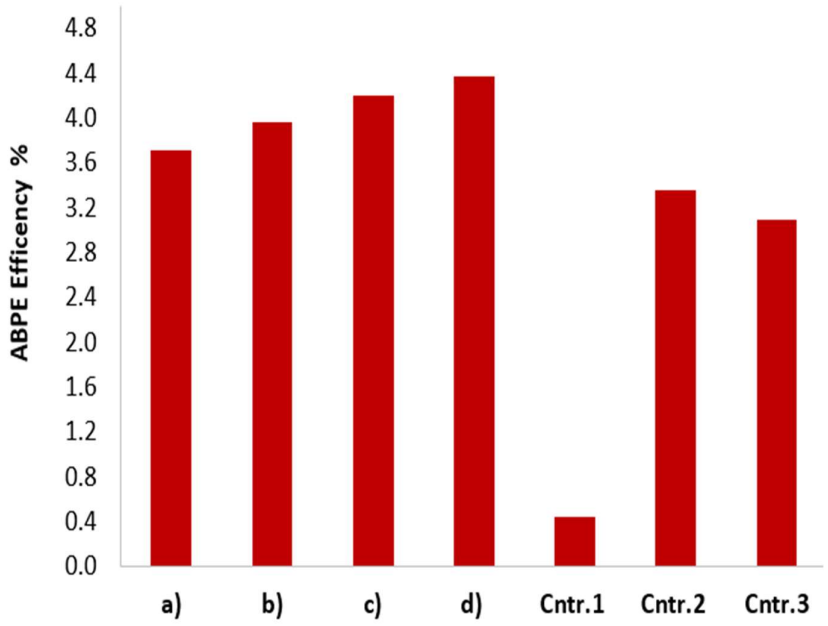

Figure 6. Applied-bias photon-to-current efficiency (ABPE) of the d) CdS–MoS_2–rGO photocathode and control films measured under identical bias and illumination conditions.

 doi:10.20944/preprints202601.2091.v1

5. Conclusions

CdS–MoS_2–rGO thin-film electrochemical -photocathode prepared a single and scalable precursor ink exhibited synergistic improvement in PEC-HER at neutral pH. The optimized 86:9:5 composition ratios shows; (i) higher photocurrent and less-negative onset potential than all other controls film, (ii) lowiceest illuminated Rct wth highest Cdl, which reflected the faster interfacial charge transfer and largest ECSA, (iii) a lowest illuminated Tafel slope around (~85 mV dec^{-1}) resulted in improved HER kinetics, (iv) a stable over 1 hour of operation with only ~4% current loss through chopped-light testing, and (v) hydrogen evolution rate verified substantially by GC. All resulting data demonstrated the cooperative mechanism within tri-composite CdS-MoS_2-rGO.Where CdS generated photo-charges carriers, rGO provided channels for electrons transmission with minimal resistive loss, and finally MoS_2 that supplied Co-catalytically competent at edge sites. CdS-MoS_2-rGO film within ration 86:9:5 respectively was optimized mechanism functions making it superior to their binary implementations.

In spite of CdS–MoS_2–rGO photocathode exhibited an excellent performance under halogen lamp illumination and maintains stability for 1 h, further investigation under standard AM 1.5G simulated sunlight as well as extend durability of testing are required to validate scalability. In addition, while CdS provides strong visible absorption, its intrinsic toxicity and photocorrosion risk could limit large-scale application unless passivation gc Environmental risk assessment and toxicological evaluation of CdS-based photocathodes will be addressed in future studies focused on long-term operation and large-scale deployment.

Supplementary Materials: The following supporting information can be downloaded at the website of this paper posted on Preprints.org.

Author Contributions: Conceptualization, investigation and methodology M.A. software, formal analysis, resources and data curation, A.S.; writing—original draft preparation, writing—review and editing and visualization, M.M.A.; supervision, project administration, H.A. All authors have read and agreed to the published version of the manuscript

Funding This research received no external funding

Data Availability Statement: The original data are presented in this study for more inquiries can be contacted corresponding author.

Acknowledgments: We thank the University of Mosul for its support.

Conflicts of Interest: The authors declare no conflicts of interest.

References

1. Xu, Y. and M.A.A. Schoonen, The absolute energy positions of conduction and valence bands of selected semiconducting minerals. American Mineralogist, 2000. 85(3-4): p. 543-556.
2. Nasir, J.A., et al., Recent developments and perspectives in CdS-based photocatalysts for water splitting. Journal of Materials Chemistry A, 2020. 8(40): p. 20752-20780.
3. Hinnemann, B., et al., Biomimetic Hydrogen Evolution: MoS_2 Nanoparticles as Catalyst for Hydrogen Evolution. Journal of the American Chemical Society, 2005. 127(15): p. 5308-5309.
4. Voiry, D., et al., Conducting MoS_2 Nanosheets as Catalysts for Hydrogen Evolution Reaction. Nano Letters, 2013. 13(12): p. 6222-6227.
5. Lu, K.-Q., et al., Roles of Graphene Oxide in Heterogeneous Photocatalysis. ACS Materials Au, 2021. 1(1): p. 37-54.
6. Hummers, W.S., Jr. and R.E. Offeman, Preparation of Graphitic Oxide. Journal of the American Chemical Society, 1958. 80(6): p. 1339-1339.

 doi:10.20944/preprints202601.2091.v1

7. Marcano, D.C., et al., Improved Synthesis of Graphene Oxide. ACS Nano, 2010. 4(8): p. 4806-4814.
8. Ortega-Borges, R. and D. Lincot, Mechanism of Chemical Bath Deposition of Cadmium Sulfide Thin Films in the Ammonia-Thiourea System: In Situ Kinetic Study and Modelization. Journal of The Electrochemical Society, 1993. 140(12): p. 3464.
9. Najm, A.S., et al., Mechanism of Chemical Bath Deposition of CdS Thin Films: Influence of Sulphur Precursor Concentration on Microstructural and Optoelectronic Characterizations. Coatings, 2022. 12(10): p. 1400.
10. Bao, N., et al., Facile Cd−Thiourea Complex Thermolysis Synthesis of Phase-Controlled CdS Nanocrystals for Photocatalytic Hydrogen Production under Visible Light. The Journal of Physical Chemistry C, 2007. 111(47): p. 17527-17534.
11. Yin, Y., et al., Contributions of Phase, Sulfur Vacancies, and Edges to the Hydrogen Evolution Reaction Catalytic Activity of Porous Molybdenum Disulfide Nanosheets. Journal of the American Chemical Society, 2016. 138(25): p. 7965-7972.
12. Mondal, A., et al., Boosting Photocatalytic Activity Using Reduced Graphene Oxide (RGO)/Semiconductor Nanocomposites: Issues and Future Scope. ACS Omega, 2021. 6(13): p. 8734-8743.
13. Ren, H., et al., Facile Solution Spin-Coating SnO_2 Thin Film Covering Cracks of TiO_2 Hole Blocking Layer for Perovskite Solar Cells. Coatings, 2018. 8(9): p. 314.
14. Weidling, A.M., et al., Large-area photonic lift-off process for flexible thin-film transistors. npj Flexible Electronics, 2022. 6(1): p. 14.
15. Kolhe, S., et al., Effects of air annealing on chemincally deposited CdS films exmained by XPS and XRD. Solar Energy Materials, 1984. 10(1): p. 47-54.
16. Allen J. Bard and Larry R. Faulkner, Electrochemical Methods: Fundamentals and Applications, New York: Wiley, 2001, 2nd ed. Russian Journal of Electrochemistry, 2002. 38(12): p. 1364-1365.
17. Vivier, V. and M.E. Orazem, Impedance analysis of electrochemical systems. Chemical Reviews, 2022. 122(12): p. 11131-11168.
18. Yan, Y., et al., Recent Development of Molybdenum Sulfides as Advanced Electrocatalysts for Hydrogen Evolution Reaction. ACS Catalysis, 2014. 4(6): p. 1693-1705.
19. Kamat, P.V., Graphene-based nanoarchitectures. Anchoring semiconductor and metal nanoparticles on a two-dimensional carbon support. The Journal of Physical Chemistry Letters, 2010. 1(2): p. 520-527.
20. Xiang, Q., B. Cheng, and J. Yu, Graphene-Based Photocatalysts for Solar-Fuel Generation. Angewandte Chemie International Edition, 2015. 54(39): p. 11350-11366.
21. Zong, X., et al., Photocatalytic H_2 Evolution on MoS_2/CdS Catalysts under Visible Light Irradiation. The Journal of Physical Chemistry C, 2010. 114(4): p. 1963-1968.
22. Seo, D.B. and T.N. Trung, Improved Photoelectrochemical Performance of MoS(2) through Morphology-Controlled Chemical Vapor Deposition Growth on Graphene. 2021. 11(6).
23. Krishna Kumar, A.S., S.J. Jiang, and J.K. Warchoł, Synthesis and Characterization of Two-Dimensional Transition Metal Dichalcogenide Magnetic MoS(2)@Fe(3)O(4) Nanoparticles for Adsorption of Cr(VI)/Cr(III). ACS Omega, 2017. 2(9): p. 6187-6200.
24. Sumair Ahmed, S., et al., Improved Performance of CuFe2O4/rGO Nanohybrid as an Anode Material for Lithium-ion Batteries Prepared Via Facile One-step Method. Current Nanoscience, 2019. 15(4): p. 420-429.
25. Maticiuc, N., et al., Structural and optical properties of cadmium sulfide thin films modified by hydrogen annealing. Materials Science in Semiconductor Processing, 2014. **26**: p. 169-174.
26. Kar, S., S. Ghosh, and T. Pal, MoS2-CdS composite for photocatalytic reduction of hexavalent chromium and thin film optoelectronic device applications. Scientific Reports, 2024. **14**(1): p. 18674.
27. Jones, L.A.H., et al., Band Alignments, Electronic Structure, and Core-Level Spectra of Bulk Molybdenum Dichalcogenides (MoS2, MoSe2, and MoTe2). The Journal of Physical Chemistry C, 2022. **126**(49): p. 21022-21033.
28. Hamid, K., M.Z. Bin Mukhlish, and M.T. Uddin, Sunlight-activated heterostructure MoS_2/CdS nanocomposite photocatalyst with enhanced photocatalytic activity: band alignment and mechanism study. RSC Advances, 2024. 14(52): p. 38908-38923.

 doi:10.20944/preprints202601.2091.v1

29. Johra, F.T. and W.-G. Jung, Hydrothermally reduced graphene oxide as a supercapacitor. Applied Surface Science, 2015. 357: p. 1911-1914.
30. Abdolahzadeh Ziabari, A. and F.E. Ghodsi, Growth, characterization and studying of sol–gel derived CdS nanoscrystalline thin films incorporated in polyethyleneglycol: Effects of post-heat treatment. Solar Energy Materials and Solar Cells, 2012. 105: p. 249-262.
31. Yan, Z., L. Du, and D. Lee Phillips, Multilayer core–shell MoS_2/CdS nanorods with very high photocatalytic activity for hydrogen production under visible-light excitation and investigation of the photocatalytic mechanism by femtosecond transient absorption spectroscopy. RSC Advances, 2017. 7(88): p. 55993-55999.
32. Yao, Y., et al., MoS_2 Coexisting in 1T and 2H Phases Synthesized by Common Hydrothermal Method for Hydrogen Evolution Reaction. Nanomaterials, 2019. 9(6): p. 844.
33. Macdonald, J.R., Impedance spectroscopy: emphasizing solid materials and systems. Applied Optics, 1989. 28(6): p. 1083.
34. Macdonald, J.R., et al., Impedance spectroscopy: theory, experiment, and applications. 2018: John Wiley & Sons.
35. Lasia, A., Electrochemical impedance spectroscopy and its applications, in Modern aspects of electrochemistry. 2002, Springer. p. 143-248.
36. Kékedy-Nagy, L., et al., An Electrochemical Study of Ammonium Dihydrogen Phosphate on Mg and Mg Alloy Electrodes. Electrocatalysis, 2021. 12(3): p. 251-263.
37. Wan, X., et al., Enhanced Photoelectrochemical Water Oxidation on $BiVO_4$ Photoanodes Functionalized by Bimetallic Dicyanamide Molecular Catalysts. Sustainability, 2023. 15(4): p. 3129.